Materials & Design 239 (2024) 112757

Contents lists available at ScienceDirect

Materials & Design

journal homepage: www.elsevier.com/locate/matdes

Device level assessment of Ni and $Ni_{45}Cu_{55}$ as electrodes in $Mg_2(Si,Sn)$-based thermoelectric generators

Radhika Deshpande [a,*], Julia Camut [a], Eckhard Müller [a,b], Johannes de Boor [a,c,*]

[a] Institute of Materials Research, German Aerospace Centre (DLR), Cologne, Germany
[b] Institute of Inorganic and Analytical Chemistry, Justus Liebig University of Giessen, Giessen, Germany
[c] Institute of Technology for Nanostructures (NST) and CENIDE, Faculty of Engineering, University of Duisburg, Essen, Germany

ARTICLE INFO

Keywords:
Mg_2Si
Thermoelectric
Electrodes
Device Modelling

ABSTRACT

Owing to efficient thermoelectric conversion, non-toxicity, low density and cost, $Mg_2(Si,Sn)$-based solid solutions hold potential for mid-to-high temperature waste heat recovery. Yet, challenges arise from n-$Mg_2(Si,Sn)$ degradation at ≥400 °C caused by Mg loss and charge carrier reduction, particularly in Sn-rich compositions. To build a thermoelectric generator (TEG) stable up to 400 °C, we propose binary Mg_2Si as the n-type leg. Using $Ni_{45}Cu_{55}$ and Ni yields low electrical contact resistance (<5 μΩ.cm^2) without altering the thermoelectric properties of n-Mg_2Si. We fabricated two 2×2 leg TE modules with the same electrode/TE combination for the p-type legs and with Ni or $Ni_{45}Cu_{55}$ for their n-type legs and tested up to 400 °C, allowing for a direct comparison between these two electrodes for n-Mg_2Si at the device level. $Ni_{45}Cu_{55}$ outperformed Ni, resulting in a peak power density of 0.79 W/cm^2 at ΔT ~375 K and an efficiency competitive to $Mg_2(Si,Sn)$-only TEG. Comparative simulations using a constant property model revealed a strong reduction of internal losses when using $Ni_{45}Cu_{55}$ as the electrode for n-Mg_2Si as the main reason for the high performance. The presented design overcame challenges such as Mg sublimation at targeted application temperature or electrode induced defect formation, resulting in a stable TEG.

1. Introduction

Climate change is one of the fundamental challenges that humanity is facing. Emission of CO_2 and other greenhouse gases by conventional use of limited resources of fossil fuels is one of the primary reasons of global warming. Evolving concerns of global warming and limited supply of fossil fuels demand alternate ways of energy conversion to fulfil consumer demands. Improving the energy efficiency of industrial production processes and automobile engines is the key to a solution. Thermoelectric heat recovery can help to limit the global warming by reducing greenhouse gas emissions, decrease the dependence of the society on fossil fuels, and secure the coverage of the rising energy demands. In contrast to other heat conversion techniques, thermoelectric generators (TEG) provide a clean energy technology for direct conversion of heat into electricity. TEG are compact and robust solid-state devices with no moving parts and do not produce any noise or vibrations making them reliable for long working duration at no maintenance. On account of these benefits, TEG have found applications in earlier deep space missions, remote data communication and navigation systems, climate-controlled seat technologies, polar weather stations, and waste heat recovery applications in aerospace and automotive industries [1–3]. Recently, in 2021, TEG have also been tested in the Bottle Rock geothermal field in the Geysers as a means of large scale utilisation of this technology [4]. Besides the aforementioned application, TEG have been implemented in wearable electrocardiographic systems which are operated by extracting human body heat for sourcing power [5].

The performance of TEG is governed by the figure of merit (ZT) of the device, which is given by Eq. (1) [6]

$$ZT = \frac{S_{dev}^2 T}{RK} = \frac{S_{dev}^2 T}{(R_{leg} + R_{para})K} \quad (1)$$

where S_{dev} is the Seebeck coefficient of the device which is the sum of average values of the Seebeck coefficients of n- and p-type thermoelectric legs employed in the device, R is the total resistance which contains the contributions from the TE legs R_{leg} and additional resistances (e.g. from contacts), summarized here as R_{para}. K is the total

* Corresponding authors.
E-mail addresses: radhika.deshpande@dlr.de (R. Deshpande), johannes.deboor@dlr.de (J. de Boor).

https://doi.org/10.1016/j.matdes.2024.112757
Received 1 December 2023; Received in revised form 3 February 2024; Accepted 13 February 2024
Available online 16 February 2024

thermal conductance of the legs K_{leg} and might also consider further parasitic heat bypasses, and T is the absolute temperature. This equation is used in the context of the Constant Property Model (CPM) [7].

Only if losses in the device are negligibly small and the p- and n-type materials are similar in their TE properties, the device ZT may be approximated, in the sense of an upper ideal limit, by the figure-of-merit zT of the TE materials, which is given by Eq. (2).

$$zT = \frac{S^2\sigma T}{\kappa} \tag{2}$$

where S, σ, T, and κ are the Seebeck coefficient, the electrical conductivity, the absolute temperature and the thermal conductivity, respectively.

A wide array of material classes is currently under exploration for their potential in achieving high thermoelectric performance [8–11]. Magnesium silicides offer a range of benefits as thermoelectric materials, including high thermoelectric figure of merit [n-type: $zT \approx 1.4$ at 450 °C [12] and p-type $zT \approx 0.55$ [13] at 350 °C], non-toxicity, low density, abundance, and affordability. They have been previously explored for use in high temperature waste heat recovery applications. Although silicide-based thermoelectric materials have been optimized at a material level through several studies [12–15] there has been limited research on the use of these materials in the development of thermoelectric modules. Three fully $Mg_2(Si,Sn)$-based TEG were reported previously. Most recently, Camut et al. reported a power density of 0.9 W/cm^2 (with respect to the area of the TE legs) and a maximum efficiency of 3.6 % for a full $Mg_2(Si,Sn)$ module [16]. Earlier, Goyal *et al.* reported a power density of 0.52 W/cm^2 (TE area) and predicted a maximum efficiency of 5 % [17]. In 2016, Gao reported a maximum power output of 0.12 W corresponding to a power density of 0.47 W/cm^2 for $T_h = 440$ °C and $T_c = 110$ °C [18]. Research has also been conducted using the more stable Mg_2Si instead of the higher performant $Mg_2(Si,Sn)$ in power generation. In a study of a segmented TEG made of BiTe and Mg_2Si/HMS [19], a maximum power density 0.8 W/cm^2 (per TE area) for $\Delta T = 498$ K and an efficiency up to 5 % for $T_h = 500$ °C, $T_c = 25$ °C have been reported. Additionally, pairing Mg_2Si with Si-Ge resulted in a power density of 1.8 W/cm^2 for $T_h = 650$ °C and $T_c = 30$ °C [20].

n-type $Mg_2Si_{1-x}Sn_x$ ($x \approx 0.7$) potentially suffers from a limited thermodynamic stability due to a miscibility gap reported for the pseudo-binary phase diagram and Mg loss [15,21–23]. As the stability against oxidation and Mg loss decreases with increasing x the unmixing at high temperatures favors oxidation in air and (local) Mg sublimation [24]. Very recent work also indicates that the stability of Mg-rich Mg-based materials might be limited already at room temperature due to a fast diffusion of Mg [25,26]. The Mg-poor p-type counterpart, on the other hand, has shown reproducibly stable thermoelectric performance [13,16,27–29]. Further research [27,30] on the contacting of magnesium silicides with various electrodes reported on a change in optimum carrier concentration of the n-type leg resulting in a suboptimal performance of the TEG. In particular, n-type $Mg_2Si_{1-x}Sn_x$ showed significant changes in the TE properties presumably due to diffusion of Ag from the electrode into the TE material [30] while no such degradation of the properties was observed with the p-type counterpart. On the other hand, binary n-Mg_2Si has shown decent TE properties with $zT_{max} > 0.7$ [31,32] and a higher stability against oxidation up to 500 °C [24,33]. Due to its good stability over a large temperature range, Mg_2Si was chosen as the n-type leg for the fabrication of TEG laboratory modules in this work. Ni was assessed as a potential electrode for Mg_2Si by de Boor et al. [34–36]. The study found out that Ni is a promising electrode which showed good adhesion and low electrical contact resistance with r_c (=$R_c \times A$ (where A is the area of cross-section) ~4.4 ± 2.7 μΩcm^2. Cu was also tested as a potential candidate for both undoped [37] and doped Mg_2Si [38]. The undoped Mg_2Si resulted in a much higher value of r_c ~13.7 mΩcm^2 than for the doped Mg_2Si which had an r_c of around 44.3 μΩcm^2.

In our pursuit of building Mg_2X TEG, we tested n-Mg_2Si with Ni and Constantan ($Ni_{45}Cu_{55}$) as potential electrodes for TE metallization in this work. We found that $Ni_{45}Cu_{55}$ and Ni might overcome the shortcomings of other electrodes (e. g., Al [28], Cu [37,39], Ag [27]) by providing a low electrical contact resistances (<10 μΩcm^2), symmetric among both the hot side and cold side interfaces without altering the intrinsic properties of the TE material. $Ni_{45}Cu_{55}$ has been employed previously for a different material system (Sn-rich $Mg_2(Si,Sn)$) [39] and was shown to be unsuitable due to the formation of cracks owing to CTE mismatch of TE with the electrode and a comparatively higher electrical contact resistance (~30 μΩcm^2), accompanied by the reduction of charge carrier concentration due to the interdiffusion of elements at the interface. Notably, its compatibility with the more stable Mg_2Si and its performance in a functioning device have not been assessed until now. This study illuminates two key facets: firstly, a comparative evaluation of two distinct electrodes at the leg level, and secondly, an exploration of electrode performance at the device level. The latter involves the analysis of these functionalized legs under thermal cycling conditions. The original approach of this study lies in its unique material combination in order to design this TEG.

To further evaluate the efficacy of these electrodes, a comparison was made at the device level between two TEG 2×2 leg devices, with p-type legs composed of $Mg_{1.97}Li_{0.03}Si_{0.3}Sn_{0.7}$ and Ag electrodes. We found that r_c of Ni on the n-type material significantly increases after dicing the metallized legs and upon TEG characterization. In contrast, the use of $Ni_{45}Cu_{55}$ as the electrode material on the n-type material resulted in interfaces with low and stable electrical contact resistances (r_c) even after dicing and through thermal cycling. The here presented design resulted in a stable TEG and overcomes the shortcomings of earlier work like Mg sublimation or electrode induced defect formation at targeted application temperatures. We find that the measured efficiency of the prototype is comparable to that of previously reported fully $Mg_2(Si,Sn)$-based TEGs due to the reduction of internal losses. The open-circuit voltage, inner electrical resistance, and maximum efficiency were measured and compared with predictions based on the constant property model.

2. Experimental

2.1. Synthesis and characterization of the TE material

The synthesis of n- and p-type thermoelectric (TE) powders was performed by using the melting route introduced in [12,27,39] with the following nominal stoichiometry: $Mg_{2.06}Si_{0.965}Bi_{0.035}$ and $Mg_{1.97}Li_{0.03}Si_{0.3}Sn_{0.7}$. The excess Mg (3 at% with respect to nominal Mg content) was added for the synthesis of $Mg_{2.06}Si_{0.965}Bi_{0.035}$ to compensate for potential Mg loss during the preparation route and to obtain nearly phase pure materials. The powders were sintered using a direct current sintering press (DSP 510 SE, Dr. Fritsch GmbH) with a heating rate of 1 K/s, and pressing conditions were optimized based on previous research to achieve optimal TE properties. Density measurements were performed using Archimedes' method, yielding a relative density of >95 % for all samples. The temperature-dependent electronic transport properties were measured using a four-probe technique in an in-house facility [40,41]. The thermal diffusivity (α) was measured using a Netzsch LFA 427 apparatus, and thermal conductivity (κ) was calculated using the relation $\kappa = \alpha\rho c_p$, where specific heat capacity (c_p) value was calculated by the Dulong-Petit law: $c_p = c_V^{DP} + \frac{9E_t^2 T}{\beta_T \rho}$, where $E_t \sim 2 \times 10^{-5}$ K^{-1} and $\beta_T \sim 2.07 \times 10^{-11}$ Pa^{-1} are the linear coefficient of thermal expansion and isothermal compressibility, respectively [14,42].

2.2. TE legs metallization

In this study, p-type TE material was joined with Ag electrode foils through a two-step sintering process at 450 °C, as reported previously in [27]. For the n-type TE, two different electrode materials were utilized,

namely constantan ($Ni_{45}Cu_{55}$, Goodfellow) and nickel (Ni foil, Alfa Aesar). $Ni_{45}Cu_{55}$ was joined by stacking foil layers on either side of the TE pellet and subjecting the stack to a high-pressure, high-temperature treatment at 700 °C and 29 MPa for 10 min in the DSP facility. In contrast, Ni was joined via a one-step sintering procedure, where Ni foil layers were placed on top and bottom of the n-type TE powder, and the entire assembly was pressed and sintered at 800 °C and 66 MPa for 10 min. The number of foil layers was chosen to allow for electrical contact resistance measurements, which have a limited lateral resolution [36,43]. The optimal compaction temperature for $Mg_2Si_{1-x}Sn_x$ depends on the solid solution composition x [13], and the suitable processing window to join the metal electrode to the TE material is also specific to both components, therefore for $Ni_{45}Cu_{55}$, a two-step process was required. The resulting metallized TE pellets were diced into legs using a Disco DAD321 automatic dicing saw, with a cutting speed of 0.3 mm/s and an angular speed of 30,000 rpm. The contact quality of these metallized TE legs was evaluated by measuring their electrical contact resistances r_c at the joining interface using an in-house-built Potential & Seebeck scanning microprobe (PSM) [43]. In order to monitor any variation in the electrical contact resistance during the dicing process, the characterization of the metallized TE elements was performed in two stages. During the dicing process, the cutting blade must traverse in both the x and y directions in order to produce legs of specified dimensions. In the first stage of characterization, each n-type pellet was characterized after a single x-cut and referred to as a "bar". In the second stage, after both x and y cuts were completed, the resulting elements were referred to as TE "legs".

2.3. Electrical contact resistances and the practical yield of the TE legs

The specific contact resistance r_c is obtained on functionalized n-type legs and bars joined with Ni or $Ni_{45}Cu_{55}$. Two r_c values can generally be obtained for each contact with two different calculation methods. In the first method, the current is assumed to be distributed uniformly across the cross section of the sample and the contacts. Thus, the current density (j) of such an ideal sample is given by $j = I/A$ and the contact resistance R_c can be calculated by using Eq. (3)

$$r_c = \frac{(V_{elec} - V_{TE,\,int})A}{I_{PSM}} \tag{3}$$

Here, $V_{elec} - V_{TE,int}$ is the drop in the two distinct electrical potential values at the interface between the electrode and the TE material. The position of the interface is identified using the drop in the Seebeck coefficient on the line scan. A is the leg cross-section and I_{PSM} is the current measured in the device.

To check for that, the specific contact resistance is also calculated following Eq. (4)

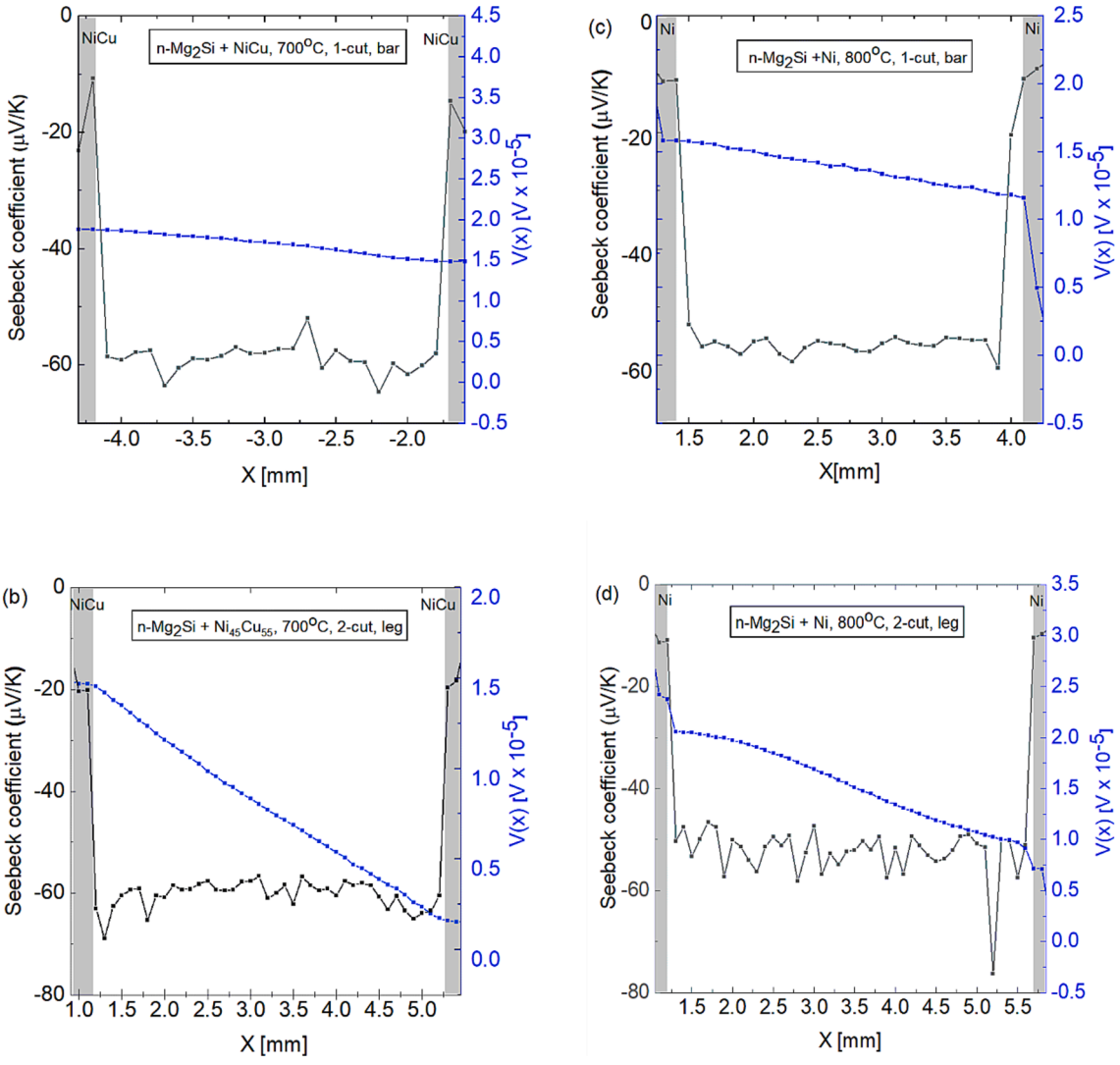

Fig. 1. Exemplary line scans of electrical potential and Seebeck coefficient for n-Mg_2Si + $Ni_{45}Cu_{55}$ (a) bar; (b) TE leg; and n-Mg_2Si + Ni (c) bar; (d) leg.

$$r_c = \frac{V_{elec} - V_{TE}}{\Delta V_{TE}} \rho_{TE} L_{TE} \quad (4)$$

where ρ_{TE} is the electrical resistivity of the TE material measured after joining (and after removing the electrodes), L_{TE} is the length of TE sample and ΔV_{TE} is the voltage drop across the TE material measured in the PSM.

Exemplary line scans of the Seebeck coefficient and potential are shown in Fig. 1 after both cutting steps, while the corresponding specific contact resistance values are given in Table 1. In this work, we report r_c values calculated by Eq. (4) and are tabulated in Table 1, as written 'left' and 'right' being the two sides of the given sample. To determine r_c, the average of all valid PSM graphs (with monotonous decrease of V_{TE} with respect to the position) was taken into account using Eq. (4). Fig. 1(a) shows that the sections of the $Ni_{45}Cu_{55}$ electrode and the TE material are distinguishable by the different Seebeck coefficient levels. The potential line scan doesn't show sudden abrupt changes inside the TE material or at the $Ni_{45}Cu_{55}/Mg_2X$ interface, indicating a good electrical connection between the electrode and TE material without cracks. Fig. 1(c) displays the PSM line scans of the Ni/n-Mg_2Si interface. For both the metals, there is no gradient in the Seebeck coefficient profile near the interface or inside the TE. This is consistent with the previous research findings [36] but different to the previously mentioned case of Ag joined to n-type Mg_2X [30]. In Fig. 1(b and d), increased scatter is observed from the PSM tip during the scanning process.

Table 1 also presents an estimated yield of TE legs. As can be seen, for both electrodes, low contact resistances are obtained after a single cut to produce bars. However, the electrical contact resistance r_c remained stable with a 100 % yield in obtaining the employable TE legs of desired dimensions from one 15 mm sample without any delamination in the n-Mg_2Si legs only for $Ni_{45}Cu_{55}$ electrodes. In contrast, the yield of TE legs was less than 25 % for the n-Mg_2Si legs joined with Ni electrodes. These exhibited an increase in r_c and the rest was lost due to delamination of Ni during the cutting process. The observed rise in r_c after the second cut in the n-Mg_2Si legs connected with Ni electrodes may be attributed to poorer adhesion during the initial contacting step as compared to $Ni_{45}Cu_{55}$. Considering the higher melting point of Ni than $Ni_{45}Cu_{55}$, poor adhesion of Ni could potentially result in micro-delamination and the formation of cracks near the interface after the first cut. During the second cut, this could contribute to the increase in r_c. The p-type legs with Ag electrodes on p-$Mg_2(Si,Sn)$, employed for the preparation of modules, displayed low electrical contact resistance values of approximately 13 $\mu\Omega cm^2$.

2.4. Module fabrication and evaluation

To furthermore assess the electrode quality on a device level, two thermoelectric generators, named TEG-1 and TEG-2, were fabricated with the primary difference being the electrode used on the n-type TE leg, $Ni_{45}Cu_{55}$ for TEG-1 and Ni for TEG-2. Both TEG prototypes had a 2×2 leg configuration with two unicouples each. The n-type and p-type TE legs were electrically joined in series and thermally connected in parallel via the use of direct-Cu bonded (DBC) substrates as the top and bottom plates, which were obtained from HHI Industrievertretungen. The legs were soldered to the DBC plates using the procedures described in [16]. The pressing parameters used in the fabrication process were a temperature of 420 °C for 15 min with a heating rate of 25 °C/min, a load of 6 kg, and a partial Argon atmosphere (~600 mbar) inside the induction furnace. We used a higher temperature of 420 °C for soldering in this work as compared to the one reported in [16] due to the higher melting temperature of $Ni_{45}Cu_{55}$ and Ni and the higher thermal stability of n-Mg_2Si compared to n-$Mg_2(Si,Sn)$. Fig. 2 shows an example of such a 2×2 TEG.

We have used a Constant Property Model (CPM) to design and evaluate the TEGs. The averaged material properties employed as input (α, ρ, thermal resistivity $1/\kappa$) are obtained by temperature averaging such as $\alpha = \frac{1}{\Delta T}\int_{T_c}^{T_h} \alpha(T)dT$, which has been shown to be accurate for Mg_2X [44]. Note that the effectively acting thermal conductivity κ_{eff} is adequately calculated as the reciprocal of the average thermal resistivity such as $\kappa_{eff} = \frac{1}{\bar{\kappa}(T)} = \left(\frac{1}{\Delta T}\int_{T_c}^{T_h} \frac{1}{\kappa(T)} dT\right)^{-1}$. Within the CPM the cross section ratio for highest efficiency, η_{max}, is given by $g_{opt_\eta} = \left(\frac{A_p}{A_n}\right)_{opt_\eta} = \sqrt{\frac{\kappa_n \sigma_n}{\kappa_p \sigma_p}}$ while for maximum power, the ratio which is given by $g_{opt\_P} = \left(\frac{A_p}{A_n}\right)_{opt_P} = \sqrt{\frac{\sigma_n}{\sigma_p}}$ [45] This gives $g_{opt\_\eta} = 2.39$ and $g_{opt\_P} = 1.56$ for $T_c = 25$ °C and $T_h = 400$ °C. As a compromise, $g = 2$ was employed practically which showed a relative loss in η_{max} of <1 %. According to this area ratio, the cross-sectional area of the n-type material measures 3.4 mm × 3.4 mm, while the p-type material has a cross-sectional area of 4.8 mm × 4.8 mm, both with a total leg length of 4.68 mm.

After the module fabrication, the module performance was measured by using an in-house built thermoelectric generator measurement apparatus (TEGMA) reported in [46–48]. The measurement was done under vacuum and an axial pressure of 1.5 MPa was applied on the TEG during the measurement. To ensure a uniform transfer of heat between all components of the measuring section, graphite foils (Dr. Fritsch Gerätebau GmbH, 200 μm) are introduced at all interfaces. The cold side temperature at the interface between TEG and measurement setup was kept constant at 25 °C, while the hot side temperature was varied within the range from 200 to 400 °C. A steady state characterization was employed during the measurement i.e. the ΔT_m step is stabilized for each current level to account for the varying Peltier heat, with a total runtime of 5 h at each target hot side temperature. It has been previously

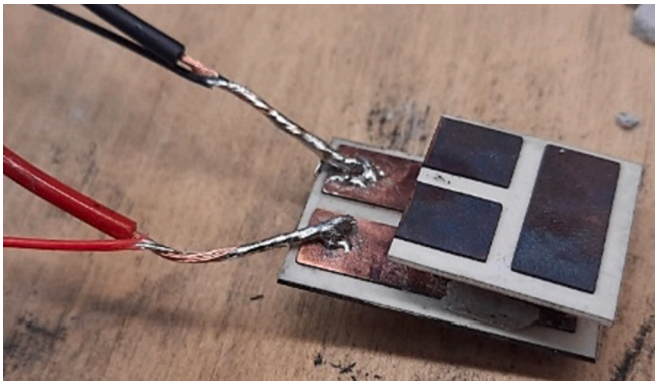

Fig. 2. Image of the TEG-1.

Table 1
Specific contact resistances (mean value ± standard deviation) of the legs used to build the module and yield.

TE	electrode	Mode of Synthesis	r_c (μΩ cm^2)				Yield of TE legs
			1-cut, bar		2-cut, TE leg		
			Left	Right	Left	Right	
$Mg_{2.06}Si_{0.965}Bi_{0.035}$	$Ni_{45}Cu_{55}$	2-step sintering	5±2	5±4	5±2	5±4	100 %
	Ni	1-step sintering	3±3	4±3	96±10	75±38	<25 %
$Mg_{1.97}Li_{0.03}Si_{0.3}Sn_{0.7}$	Ag	2-step sintering	N/A	N/A	13±10	14±8	100 %

shown in [16] that the cold and hot side temperatures are not equal to the actual temperatures at the ends of the TE legs, as there are temperature drops e.g. across the graphite foils and DBC substrates.

To make precise calculations of the module performance, first, the effective temperature boundary conditions are evaluated at open circuit ($I = 0$) and then at closed circuit conditions ($I \neq 0$) since most TEG parameters are relevant under (optimum) current flow. Using the open-circuit voltage, the effective temperature difference across TE legs, $\Delta T_{\mathrm{TE},I_0}$ can be evaluated by Eq. (5).

$$V_0 = N(\alpha_n + \alpha_p)\Delta T_{\mathrm{TE},I_0} \tag{5}$$

where N is the number of uni-couples and α_n, α_p are the average Seebeck coefficients. The temperatures measured at the outer module interfaces are initially used to obtain average values for α_n and α_p. These average values are then used to calculate the effective $\Delta T_{\mathrm{TE},I_0}$, from the open-circuit voltage (V_0). The calculated $\Delta T_{\mathrm{TE},I_0}$ is then used to determine a new temperature range, over which another average is taken. This iteration is continued until the difference between two iterations is <1 K. This effective $\Delta T_{\mathrm{TE},I_0}$ is then further used to calculate $\Delta T_{\mathrm{TE},I_{opt}}$ at optimum current flow in close-circuit loop by taking in account the Peltier heat as explained in [16]. Basically, in this method, parasitic temperature drops at the material layers and interfaces between the TE legs and the heat flow meter (HFM)/heater are considered. By considering the total parasitic temperature drop ΔT_{par}, a temperature difference $\Delta T_{\mathrm{par},I_0}$ at I = 0 and at optimum current when power is maximum $\Delta T_{\mathrm{par},I_{opt}}$ are defined. Assuming constant thermal resistance of the parasitic layers with current, ΔT_{par} varies proportionally to the heat flow. Therefore,

$(\dot{Q}_{\mathrm{opt,m}}/\dot{Q}_{0,\mathrm{m}}) = (\Delta T_{\mathrm{par},I_{opt}}/\Delta T_{\mathrm{par},I_0}) = (\Delta T_{\mathrm{m},I_{\mathrm{opt}}} - \Delta T_{\mathrm{TE},I_{\mathrm{opt}}})/\Delta T_{\mathrm{par},I_0}$

where $\dot{Q}$ is the measured heat flow and ΔT_m (= T_h – T_c as measured by TEGMA) and subscripts '0' and 'opt' refer to parameters at open-loop conditions and at optimum current for maximum power. $\Delta T_{\mathrm{par},I_0}$ is known as $\Delta T_{\mathrm{par},I_0} = \Delta T_{\mathrm{m},I_0} \Delta T_{\mathrm{TE},I_0}$. $\Delta T_{\mathrm{TE},I_{\mathrm{opt}}}$ is then calculated by using above equation, and the corresponding hot and cold side temperatures, $T_{\mathrm{h,TE,opt}}$ and $T_{\mathrm{c,TE,opt}}$ are determined. A reference by Camut et.al. [16] can be used for a full didactic method describing the assumption of symmetrical temperature loss and additional methods for determining effective temperature conditions at the TE legs using measured heat flow. It results in the decrease of ΔT_{TE} as compared to the open-loop condition.

Once the true temperatures across the TE material are obtained for $I \neq 0$, they can be taken forward for calculation of TEG performance. We use CPM for all our calculations and within this model, the heat flow at maximum power $\dot{Q}_{\mathrm{opt}}$ is calculated using Eq. (6)

$$\dot{Q}_{\mathrm{opt}} = K_{\mathrm{TE}}\Delta T_{\mathrm{TE,opt}} + I \bullet N \bullet (\alpha_p - \alpha_n) T_{\mathrm{h,TE,opt}} - \frac{1}{2} I^2 R \tag{6}$$

It has three constituents of heat flow as indicated: Fourier heat flow related to thermal conduction, Peltier heat and Joule heat due to the current flow in the circuit. The electrical resistance is given by Eq. (7)

$$R = R_{\mathrm{TE}} + R_c + R_{\mathrm{Cu}} = N\left[\frac{\rho_p L}{A_p} + \frac{\rho_n L}{A_n} + \frac{2r_{cp}}{A_p} + \frac{2r_{cn}}{A_n}\right] + \sum \frac{L_i}{\sigma_{\mathrm{Cu}}(T) A_i} \tag{7}$$

where R_{TE} is the total electrical resistance of the TE legs and R_c the total electrical contact resistance and R_{Cu} is the total resistance of Cu on the DBC plate. The latter is calculated as a series addition of two stripes at the top ($L_1 = 1.2$ cm) and three stripes at the bottom of the DBC plate ($L_1 = 1.2$ cm and $L_2 = 1.6$ cm) each with a thickness of 250 μm and 0.5 cm in width. The temperature-dependent electrical conductivity of Cu [$\sigma_{\mathrm{Cu}}(T)$] was referred from [49]. Furthermore, the thermal conductance of the TEG is given by Eq. (8)

$$K_{\mathrm{TE}} = N\left(\frac{\kappa_p A_p}{L} + \frac{\kappa_n A_n}{L}\right) \tag{8}$$

The maximum power output, P_{max} of TEG is given in CPM by Eq. (9)

$$P_{\mathrm{max}} = \frac{\left(N(\alpha_p - \alpha_n)\Delta T_{\mathrm{TE,opt}}\right)^2}{4R} \tag{9}$$

and the conversion efficiency is given by the following Eq. (10) in terms of device figure of merit ZT, (refer Eq. (1))

$$\eta_{\mathrm{max}} = \frac{T_{\mathrm{h,TE,\ opt}} - T_{\mathrm{c,TE,opt}}}{T_{\mathrm{h,TE,\ opt}}} \frac{\sqrt{1+ZT} - 1}{\frac{T_{\mathrm{c,TE,opt}}}{T_{\mathrm{h,TE,\ opt}}} + \sqrt{1+ZT}} \tag{10}$$

3. Results

3.1. Microstructural analysis of Ni vs. $Ni_{45}Cu_{55}$ electrodes on n-Mg_2Si

The SEM images of the interface and near-interface regions of the n-Mg_2Si TE material joined to $Ni_{45}Cu_{55}$ and Ni are presented in Fig. 3. The interface of the TE material with $Ni_{45}Cu_{55}$ exhibits a mottled structure, which is similar to the microstructure reported in [39] for the interface of n-$Mg_2(Si,Sn)$ with Cu. Presumably due to the lack of Sn in the present case, the interface is not as complex and there are fewer phases present. The interdiffusion zone consists of the main layer of 20 μm thickness with some tendrils extending roughly about ~50 μm. The EDX-approximated composition of the interface layers between the TE material and $Ni_{45}Cu_{55}$ is suggested as $Mg_{1.2}NiCu_2$ on Fig. 3(b), indicating a gradual change in Cu content from the electrode to the TE material. It looks like the lower Cu-free layer, approximated to the composition of Mg_3SiNi_5 may act as the barrier between Cu and the TE material as Cu presence was not detected by EDX beyond the first reaction layer as mentioned above. Ayachi et al. [39] investigated the behavior of $Ni_{45}Cu_{55}$ as an electrode for $Mg_2Si_{0.3}Sn_{0.7}$ solid solutions. They observed a thick reaction layer containing distinct ternary phases, including compositions of Cu, Mg and Sn in one layer, and Ni and Si-rich accumulations in the next layer. This Ni-Si phase formation has been previously documented in Mg_2Si/Ni contacts where a single reaction layer of $Ni_{31}Si_{12}$ was identified. Additionally, the ternary phases Mg_2SiNi_3 and Ni_2Mg were reported [50]. SEM/EDX analysis of the n-type TE with a $Cu_{55}Ni_{45}$ electrode in this work, revealed the formation of ternary phases of Mg, Si, and Ni with a gradual change of Ni, the compositions being approximated such as Mg_3SiNi_5 and Mg_2SiNi_3, and a ternary composition of Mg and Ni with Cu, as $Mg_{1.2}NiCu_2$ in the distinct reaction layers (Fig. 3b). It is plausible that these EDX-approximated compositions can be an overlay of intermixed or adjacent phases. A liquid phase is also indicated in Mg-Cu [51] phase diagrams, can be a hint for the tailing near the mottled structure (Fig. 3b) growing locally inside the TE material.

On the other hand, Ni forms a growing "rod-like " interface with Mg_2Si (Fig. 3d), clearly different from that of Mg_2Si with $Ni_{45}Cu_{55}$. There are three distinct reaction layers. The thickness of the interface region close to the electrode is 20 μm thick growing upto approximately 100 μm in the form of rod-like structure. The compositions of the interface layers, as acquired by EDX point analysis, are given in the Fig. 3d and were approximated as $NiSi_4$ in the first layer which can be seen by the gradient in grey scale, $MgSi_{2.66}Ni_{1.1}$ in the second layer, and the rods or lamellae consist of $Mg_{1.2}SiNi_{1.2}$. EDX point analyses at different spots in the region show an interdependent gradual change in Ni, Si and Mg as we move from the electrode to the TE material on the interface. In contrast to the formation of ternary phases at the interface of $Ni_{45}Cu_{55}$ to n-type TE material, the interface of Ni to the n-type TE showed the presence of three distinct reaction layers. This observation is consistent with previous studies by de Boor et al. [35,36] who reported similar ternary compositions at the interface. As the possibility of an overlay of intermixed or adjacent phases cannot be avoided but from the binary phase diagrams of Mg-Ni [52], a liquid phase is indicated above 508 °C which is above the joining temperature of Ni. This may be a probable explanation for the growing rod-like structure. Large cracks

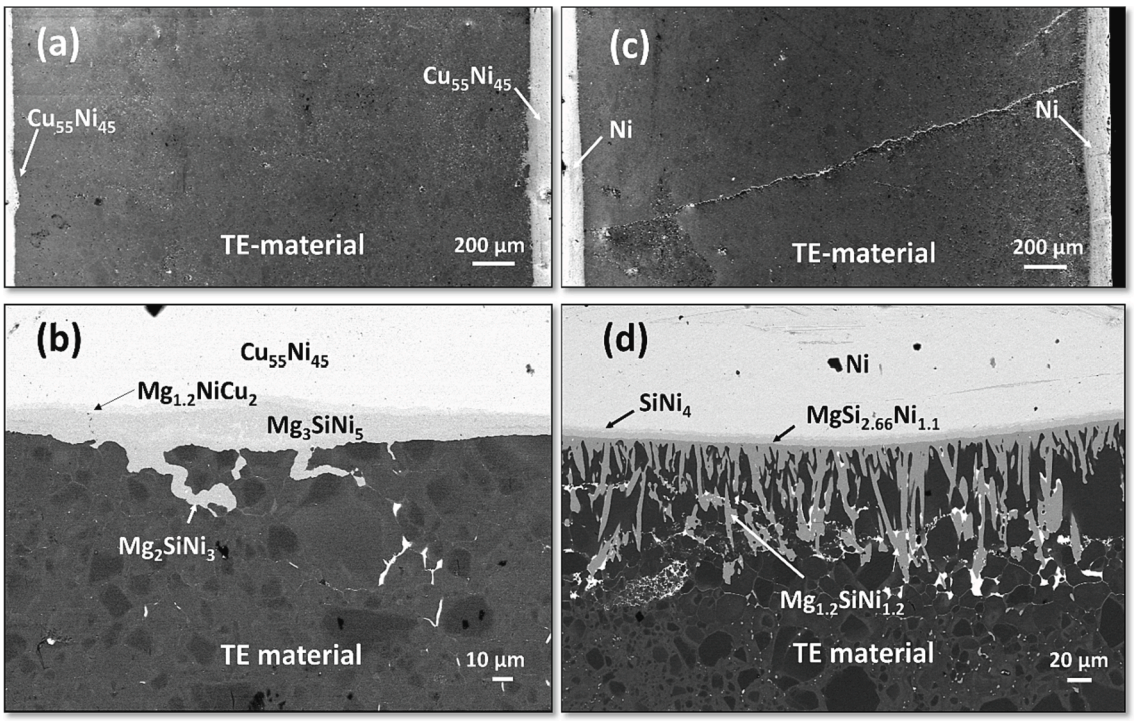

Fig. 3. SEM images of n-Mg_2Si/$Ni_{45}Cu_{55}$ (a, b) and n-Mg_2Si/Ni (c, d)(after the first cut). The indicated compositions are obtained by EDX point analysis.

were observed at various regions inside the TE material when joined with Ni, as shown in Fig. 3. The dark areas seen in the contrast within Mg_2Si have been previously reported by [50] and were there attributed to the presence of Mg-rich Mg_2Si regions.

3.2. Module measurement

Fig. 4 shows the power parabolae of TEG-1 and TEG-2, respectively. For TEG-1 in Fig. 4(a), $P(I)$ is shown for two heating and cooling cycles of the hot side temperature while for TEG-2 (Fig. 4(b)) only heating data is shown as the module broke during the measurement. The maximum power output of TEG-1 is ~0.55 W which is more than 20 times larger than that of TEG-2. The inferior performance of TEG-2 compared to TEG-1 can likely be attributed to the cracks observed in the SEM images in Fig. 3 and the increased electrical contact resistance. To gain a better understanding of the potential degradation mechanism the total internal resistance across the module is determined.

The inner resistance of the modules is determined from the calculated resistances of the TE materials for the true temperatures (explained in section 2.3), corrected for the small changes in the temperatures with increasing current as outlined in [16,46]. The total inner electrical resistance of the TE module can be estimated by using Eq. (7).

Fig. 5(a – c) compare calculated and measured values of the total resistances and open circuit voltages of TEG-1 and TEG-2 at the given temperatures. Fig. 5(a and b) are separated from each other as Fig. 5(a) indicates all calculated values in comparison to only one measured cycle

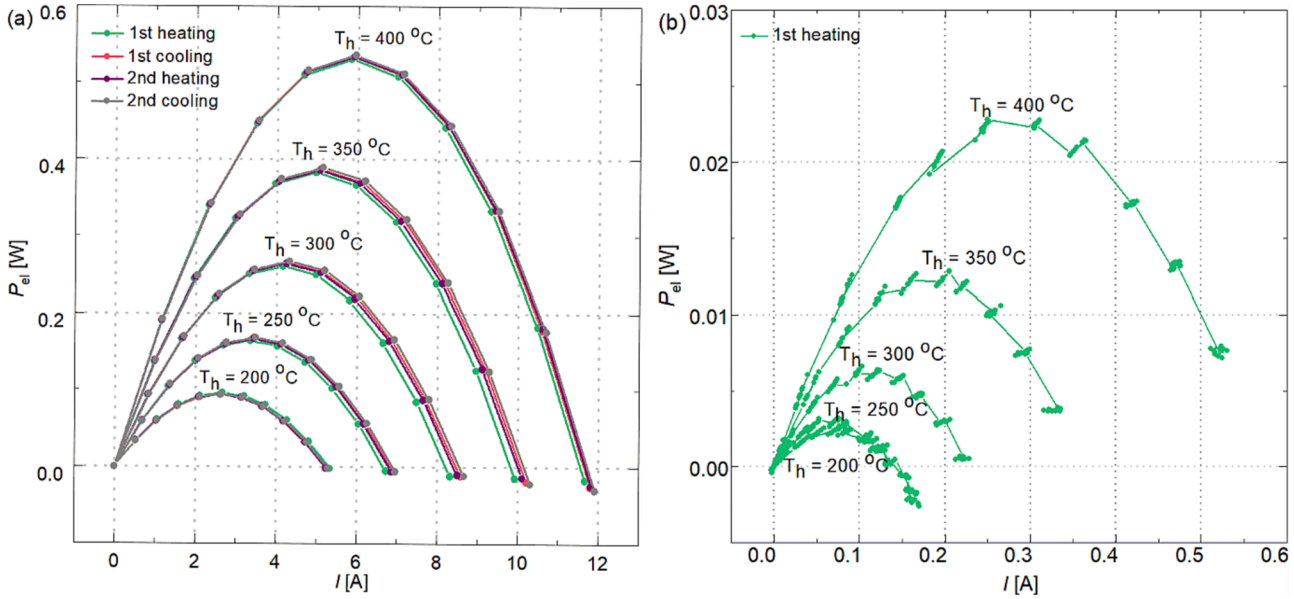

Fig. 4. Power parabolic of 2×2 TEG modules of (a) TEG-1 (joined with $Ni_{45}Cu_{55}$ on n-leg); (b) TEG-2 (joined with Ni on n-leg).

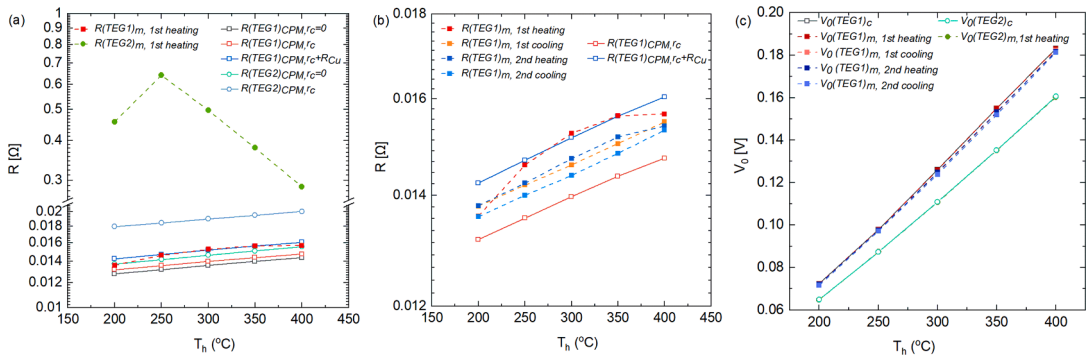

Fig. 5. Comparison of (a) R_i with 1st measured heating curves of TEG-1 and TEG-2; (b) Evolution of two measurement cycles of TEG-1 (c) V_0 of TEG-1 and TEG-2 versus hot side temperature. For TEG-2, V_0 (TEG-2)c and V_0 (TEG-2)m coincide; for legends symbols, see text.

from each, TEG-1 and TEG-2. On the other hand, Fig. 5(b) shows two full measurement cycles of TEG-1 and the data is compared with calculation. The calculated and measured values are indicated by R(TEG-j)$_{CPM}$ and R(TEG-j)$_m$, for both TEG-1 and TEG-2. Due to employing a steady state measurement, R(TEG-j)$_m$ can be extracted directly as the slope from the measured V-I curves for each temperature. The calculations compare the cases of ideal ($r_c = 0$), pre-assembly r_c (measured on contacted single legs, see Table 1) and additionally considering the resistance of the Cu bridges (R_{Cu}). As we see in Fig. 5(a), the resistance of TEG-2 is (at $T_h = 400^\circ C$) approximately twenty times higher than the expected one, R(TEG2)$_{CPM}$, r_c, indicating a significant influence of additional resistances due to e.g. cracks in the material or at the interface, as observed in Fig. 3 and a poor adhesion of Ni electrode resulting in a poor yield. The evolution of TEG-1 resistance under temperature cycling is also shown in order to see its rate of change and it can be seen that the two measured cycles are overlapping with a relative change < 2 %. In the most realistic calculation scheme, involving measured leg contact resistance and Cu bridge resistance (R(TEG1)$_{CPM}$, r_{c+RCu}), there is very good agreement between calculation and measurement, whereas lower values are calculated when neglecting bridge and contact resistance, showing the potential for improvement with respect to inner resistive losses.

While taking a look at the measured V_0 for TEG-1 and TEG-2, Fig. 5 (c), the curves of both TEG don't overlap. According to Eq. (5), V_0 depends on the average Seebeck coefficients, α_n, α_p and the effective ΔT_{TE} across TE legs. Fig. 5b shows an almost unchanged V_0 for different measurement cycles of TEG-1, indicating negligible alteration of TE properties from cycle to cycle. Although the p-type legs of both modules have a relative difference of <10 % in their Seebeck coefficients owing to different synthesis batches of p-type powders (*refer* S1), this will not explain the full amount of the difference of V_0 between both TEG. The remaining difference is likely a result of individually varying interface properties and partly delamination or cracking at the contacts (*see* Fig. 3).

Fig. 6 (a and b) shows the comparison of measured and calculated maximum power output, P_{max}, and maximum conversion efficiency, η_{max}, respectively for both TEG as a function of the hot side temperature, T_h, taking the temperatures at the TE legs for the CPM results into account. Calculations include ideal ($r_c = 0$), pre-assembly r_c (*see* Table 1) and additionally considering the resistance of the Cu bridges (R_{Cu}). All the calculations are done for the first heating cycle. TEG-1 reaches the highest calculated P_{max} for the ideal case, (TEG1)$_{CPM}$,$r_{c=0}$ followed by (TEG1)$_{CPM}$,r_c (*see* Fig. 6(a)). The calculated temperature-dependent P_{max} values with the measured electrical resistance, (TEG1)$_{CPM}$,$_{R=Rm}$ coincide well with the P_{max} calculated by considering the resistance of Cu bridges, (TEG-1)$_{CPM}$, r_c $_{+RCu}$. Comparison with measurement shows about 7 % lower power output than the ideal case, (TEG1)$_{CPM}$, $r_{c=0}$; 4 % lower than (TEG1)$_{CPM}$,r_c and a very good agreement with the calculated (TEG1)$_{CPM}$,$_{R=Rm}$. However, the measurement values during two cycles are stable. We have stable open-circuit voltage (Fig. 5(b)) and stable inner resistance (Fig. 5(a)) resulting in a stable measured power output during the cycling. On the other hand, the measured power curve for TEG-2 is very low due to high contact resistance reaching only ~0.025 W at 400 °C.

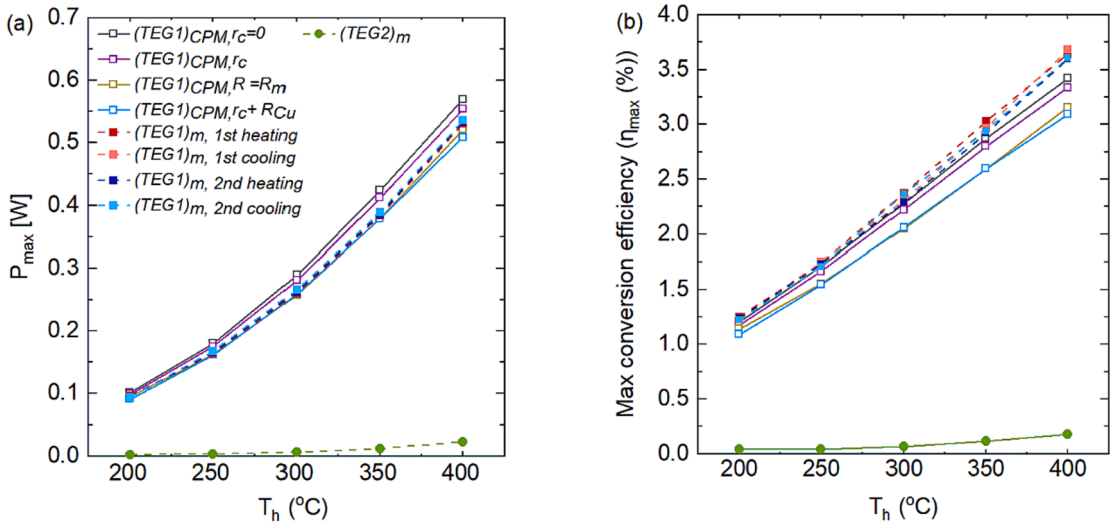

Fig. 6. Comparison between measurement and calculations using contact resistance measured on the metallized legs before TEG assembly and using contact resistance obtained from measured inner resistance, for: a) maximum power output; (b) maximum conversion efficiency.

The predicted theoretical efficiency for TEG-1 and TEG-2 at ΔT_m = 375 °C ($\Delta T_m = T_h - T_c$, as measured by TEGMA) is 3.35 % and 2.58 %, respectively. The predicted efficiency values of both TEGs differ from each other only due to their distinct r_c of the n-type TE legs (*see* Table 1) and slightly different average TE properties of the p-type legs (*refer* S1). For TEG-1, comparison of calculated values with measurement shows the same order as that in the power calculation. The difference worth to note here is that the measured efficiency is about 15 % higher than $(TEG1)_{CPM,R=Rm}$. In contrast to power measurements, efficiency measurements account for uncertainty related to heat flow during high-temperature measurements. Previous studies on TEGMA measurement techniques have reported a heat flow uncertainty of 10–13 % [46]. For the employed small TEG, the uncertainty might be larger. Fig. 6(b) displays the results of two measurement cycles of heating and cooling (in dotted lines). The conversion efficiency remains stable throughout the cycles indicating a robust design of the TEG-1. TEG-2 on the other hand, presents a curve of low efficiency over the whole temperature range (<0.25 % for ΔT_m = 375 °C) indicative for a poor and unstable design.

4. Discussion

In this work, we report the behavior of constantan ($Ni_{45}Cu_{55}$) and Ni as electrodes for n-Mg_2Si under thermal cycling and load. This section first discusses the microstructural aspect of each of these two electrodes at the interface to the TE legs during joining (see Fig. 3) and the resulting contact resistance (Table 1) during the cutting steps followed by a comparison of the two assembled TEGs in terms of their power output at optimum current.

As seen from the SEM imaging (Fig. 3), the $Ni_{45}Cu_{55}$ electrode shows good adhesion to the TE material and a crack-free zone in the TE material adjacent to the contact. Contrary to it, as joined with Ni (Fig. 3(c)), there are in-depth cracks. This is in contrast to the previously reported research by de Boor et al. [36]. The different factors in our work from [36] are the dopants for the TE material and the sintering parameters. In this work, n-type Mg_2Si is doped by 3.5 at.% Bi (at the Si position) and sintered at 800 °C while de Boor et al. used 1.25 at.% Sb dopant and sintered the material at 900 °C. The joining temperature of Ni to n-type Mg_2Si is 800 °C and with respect to its CTE, Ni is closer to Mg_2Si than the solid solution composition reported by Pham et al. [27]. The CTE of Mg_2Si is $13\times10^{-6}K^{-1}$ [53] and that of Ni [36] is also around $13\times10^{-6}K^{-1}$. On the other hand, the CTE of $Ni_{45}Cu_{55}$ as reported is $14.9\times10^{-6}K^{-1}$ [39]. Despite a larger CTE mismatch with $Ni_{45}Cu_{55}$, the joining results in a high interface adhesion with n-Mg_2Si in addition to a crack-free zone in the TE material, making $Ni_{45}Cu_{55}$ a better suitable electrode choice for n-Mg_2Si than Ni. It should also be noted that the contact resistance of the functionalized legs was initially very low (<10 $\mu\Omega cm^2$) also in this study and the main degradation appeared at the device level, a step not achieved in earlier work. This might indicate that characterization on a single leg level is insightful [54,55], but device level tests are more telling due to a longer preparation history and as the mechanical load situation related thermal cycles in a module, even related to assembly, is more complex than in a single leg [16].

Measured open circuit voltage (Fig. 5(c)) and total inner electrical resistance (Fig. 5(a and b)) show that TEG-2 contains additional electrical and thermal resistances as compared to TEG-1, resulting in a very low power output. Both TEG are measured with a cold side temperature of 25 °C and a hot side temperature of 400 °C. TEG-1 reached a power output of approximately 0.55 W at an optimal current of 5.58 A, with a deviation of <0.4 % between the measurement cycles.

Our previous work reports the first efficiency measurement of a fully $Mg_2(Si,Sn)$-based TEG reaching 3.6 % efficiency and a power output of 0.9 W/cm^2 [16]. These values are well within the range of reported silicide-based modules. However, the $Mg_2(Si,Sn)$ n-type legs showed performance degradation, presumably due to Mg loss by sublimation and electrode-induced defect formation in the TE material. In the current work, we have obtained an improved thermal and mechanical stability of the n-type leg by substituting $Mg_2Si_{1-x}Sn_x$ by Mg_2Si. Given the superior stability of Mg_2Si as evidenced by previous research [24,33], it exceeds that of $Mg_2Si_{1-x}Sn_x$, where significant degradation occurs above 400 °C [56]. Consequently, our expectation was for an enhanced stability in Mg_2Si-based TEG compared to the n-type $Mg_2Si_{1-x}Sn_x$ leg employed in fabricating a full $Mg_2(Si,Sn)$ TEG, as reported in our prior work [16]. We have achieved an excellent match between the measured and expected resistances (Fig. 5(a and b)) as there are no cracks occurring at the interface or inside the TE material (in contrast to the previous case of $Mg_2Si_{1-x}Sn_x$ [16]) due to employing a TE material with higher thermal stability. Fig. 4, Fig. 5 and Fig. 6 show a stable thermal cycling behavior of the TEG-1 up to 400 °C. We also overcame the defect diffusion issue [16] in the TE material by using the better suited $Ni_{45}Cu_{55}$ for metallization of n-Mg_2Si. Overall, this design of the TEG resulted in a similar power density of ~0.79 W/cm^2 (0.55 W) at 400 °C, a comparable efficiency (3.6 %) at a slightly longer length of TE legs and significantly worse n-type TE properties as compared to the only previously published fully $Mg_2(Si,Sn)$-made module [16].

5. Conclusions

In this article we presented a comparative device level assessment of two potential electrodes, $Ni_{45}Cu_{55}$ and Ni for n-Mg_2Si in an effort to build a robust TEG module. In conclusion, $Ni_{45}Cu_{55}$ has resulted in a better performance than Ni for n-Mg_2Si at the device level. With $Ni_{45}Cu_{55}$, the contact resistance of the n-type leg of the TEG is similar on both sides and is lower than 5 $\mu\Omega cm^2$. It remains stable during the cutting steps of the functionalized wafer into single TE legs resulting in 100 % cutting yield. No cracks were observed on $Ni_{45}Cu_{55}$/n-Mg_2Si functionalized TE legs, in contrast to the case of Ni electrode that resulted in <25 % cutting yield with large cracks inside the TE material and higher contact resistance. A module lab prototype with the $Ni_{45}Cu_{55}$ electrode has demonstrated much better performance and stability compared to one with Ni electrode. As $Ni_{45}Cu_{55}$ was contacted at 700 °C, annealing tests at lower temperatures may not result in significant changes. This bodes well for the long-term stability of the module. With $Ni_{45}Cu_{55}$ in combination to n-Mg_2Si we have demonstrated a similar performance with a power density of ~0.79 W/cm^2 as compared to a full $Mg_2(Si,Sn)$ module due to lower resistive losses, a crack-free microstructure, and an unchanged n-type material as revealed by CPM calculus analysis. Thus, we have fabricated a module featuring a novel material combination, addressing the limitations of our previous work and successfully mitigating concerns related to Mg sublimation or electrode induced defect formation.

CRediT authorship contribution statement

Radhika Deshpande: Methodology, Validation, Formal analysis, Investigation, Writing – original draft, Visualization. **Julia Camut:** Validation. **Eckhard Müller:** Writing – review & editing, Supervision. **Johannes de Boor:** Conceptualization, Methodology, Writing – review & editing, Supervision, Project administration.

Declaration of competing interest

The authors declare that they have no known competing financial interests or personal relationships that could have appeared to influence the work reported in this paper.

Data availability

Data will be made available on request.

Acknowledgements

The authors would like to gratefully acknowledge the endorsement for the DLR Executive Board Members for Space Research and Technology, as well as the financial support from the Young Research Group Leader Program. J.d.B. was supported by the Deutsche Forschungsgemeinschaft (DFG, German Research Foundation), project number 396709363. We would also like to thank Pawel Ziolkowski and Przemyslaw Blaschkewitz from DLR for their assistance with and discussions on the thermoelectric measurements. The authors would like to convey their genuine thanks for the guidance and support given by Aryan Sankhla in crafting a creative graphical abstract.

Appendix A. Supplementary data

Supplementary data to this article can be found online at https://doi.org/10.1016/j.matdes.2024.112757.

References

[1] L.E. Bell, Cooling, heating, generating power, and recovering waste heat with thermoelectric systems, Science 321 (5895) (2008) 1457–1461, https://doi.org/10.1126/science.1158899.
[2] D.K. Aswal, R. Basu, A. Singh, Key issues in development of thermoelectric power generators: High figure-of-merit materials and their highly conducting interfaces with metallic interconnects, Energy Conversion and Management 114 (2016) 50–67, https://doi.org/10.1016/j.enconman.2016.01.065.
[3] Priya S., D.J. Inman. *Energy harvesting technologies*. 21. 2009. Springer.
[4] K. Li, et al., Thermoelectric power generator: Field test at Bottle Rock geothermal power plant, Journal of Power Sources 485 (2021) 229266, https://doi.org/10.1016/j.jpowsour.2020.229266.
[5] M. Dargusch, W.-D. Liu, Z.-G. Chen, Thermoelectric Generators: Alternative Power Supply for Wearable Electrocardiographic Systems, Advanced Science 7 (18) (2020) 2001362, https://doi.org/10.1002/advs.202001362.
[6] Rowe D., *Conversion efficiency and figure-of-merit*. 1995. 31.
[7] Ioffe A.F., *Semiconductor Thermoelements, And, Thermoelectric Cooling*. 1958. Infosearch.
[8] J. He, T.M. Tritt, Advances in thermoelectric materials research: Looking back and moving forward, eaak9997, Science 357 (6358) (2017), https://doi.org/10.1126/science.aak9997.
[9] B. Jiang, et al., High figure-of-merit and power generation in high-entropy GeTe-based thermoelectrics, Science 377 (6602) (2022) 208–213, https://doi.org/10.1126/science.abq5815.
[10] X. Shi, L. Chen, C. Uher, Recent advances in high-performance bulk thermoelectric materials, International Materials Reviews 61 (6) (2016) 379–415, https://doi.org/10.1080/09506608.2016.1183075.
[11] B. Feng, et al., Preparation, Structure, and enhanced thermoelectric properties of Sm-doped BiCuSeO oxyselenide, Materials & Design 185 (2020) 108263, https://doi.org/10.1016/j.matdes.2019.108263.
[12] N. Farahi, et al., High efficiency Mg 2 (Si, Sn)-based thermoelectric materials: scale-up synthesis, functional homogeneity, and thermal stability, RSC Advances 9 (40) (2019) 23021–23028, https://doi.org/10.1039/C9RA04800F.
[13] H. Kamila, et al., Synthesis of p-type Mg2Si1-xSnx with x= 0–1 and optimization of the synthesis parameters, Materials Today: Proceedings 8 (2019) 546–555, https://doi.org/10.1016/j.matpr.2019.02.052.
[14] A. Sankhla, et al., Mechanical Alloying of Optimized Mg2(Si, Sn) Solid Solutions: Understanding Phase Evolution and Tuning Synthesis Parameters for Thermoelectric Applications, ACS Applied Energy Materials 1 (2) (2018) 531–542, https://doi.org/10.1021/acsaem.7b00128.
[15] M. Yasseri, et al., Solid solution formation in Mg2(Si, Sn) and shape of the miscibility gap, Acta Materialia 185 (2020) 80–88, https://doi.org/10.1016/j.actamat.2019.11.054.
[16] Camut, J., et al., *Efficiency Measurement and Modeling of a High-Performance Mg2(Si, Sn)-Based Thermoelectric Generator*. Advanced Engineering Materials. **n/a**(n/a): p. 2200776. https://doi.org/10.1002/adem.202200776.
[17] G.K. Goyal, T. Dasgupta, Fabrication and testing of Mg2Si1-xSnx based thermoelectric generator module, Materials Science and Engineering: B 272 (2021) 115338, https://doi.org/10.1016/j.mseb.2021.115338.
[18] Gao, P., *Mg 2 (Si, Sn)-based thermoelectric materials and devices*. 2016: Michigan State University.
[19] Kaibe, H., et al. *Development of thermoelectric generating stacked modules aiming for 15% of conversion efficiency*. in *ICT 2005. 24th International Conference on Thermoelectrics, 2005.* 2005. IEEE. doi: 10.1109/ICT.2005.1519929.
[20] Tohei T., et al. Bondability of Mg2Si element to Ni electrode using Al for thermoelectric modules. in IOP Conference Series: Materials Science and Engineering. 2014. IOP Publishing. DOI 10.1088/1757-899X/61/1/012035.
[21] M. Yasseri, et al., Influence of Mg loss on the phase stability in Mg2X (X = Si, Sn) and its correlation with coherency strain, Acta Materialia 208 (2021) 116737, https://doi.org/10.1016/j.actamat.2021.116737.
[22] R. Orenstein, et al., Using phase boundary mapping to resolve discrepancies in the Mg2Si–Mg2Sn miscibility gap, Journal of Materials Chemistry A 9 (11) (2021) 7208–7215, https://doi.org/10.1039/D1TA00115A.
[23] I.-H. Jung, et al., Thermodynamic modeling of the Mg–Si–Sn system, Calphad 31 (2) (2007) 192–200, https://doi.org/10.1016/j.calphad.2006.12.003.
[24] G. Skomedal, et al., Methods for enhancing the thermal durability of high-temperature thermoelectric materials, Journal of Electronic Materials 43 (2014) 1946–1951, https://doi.org/10.1007/s11664-013-2917-0.
[25] Duparchy A., Deshpande R., Sankhla A., Ghosh S., Camut J., Park S., Park SD, Ryu B., Mueller E., de Boor J. , *Instability mechanism in thermoelectric Mg2(Si,Sn) and the role of Mg diffusion at room temperature*. Small Science, accepted 2023.
[26] A. Li, et al., Chemical stability and degradation mechanism of Mg3Sb2-xBix thermoelectrics towards room-temperature applications, Acta Materialia 239 (2022) 118301, https://doi.org/10.1016/j.actamat.2022.118301.
[27] N.H. Pham, et al., Ni and Ag electrodes for magnesium silicide based thermoelectric generators, Materials Today Energy 11 (2019) 97–105, https://doi.org/10.1016/j.mtener.2018.10.016.
[28] J. Camut, et al., Aluminum as promising electrode for Mg2 (Si, Sn)-based thermoelectric devices, Materials Today Energy 21 (2021) 100718, https://doi.org/10.1016/j.mtener.2021.100718.
[29] J. Camut, et al., Overcoming asymmetric contact resistances in al-contacted Mg2 (Si, sn) thermoelectric legs, Materials 14 (22) (2021) 6774, https://doi.org/10.3390/ma14226774.
[30] S. Ayachi, et al., On the relevance of point defects for the selection of contacting electrodes: Ag as an example for Mg2(Si, Sn)-based thermoelectric generators, Materials Today Physics 16 (2021) 100309, https://doi.org/10.1016/j.mtphys.2020.100309.
[31] S.K. Bux, et al., Mechanochemical synthesis and thermoelectric properties of high quality magnesium silicide, Journal of Materials Chemistry 21 (33) (2011) 12259–12266, https://doi.org/10.1039/C1JM10827A.
[32] J. de Boor, et al., Fabrication parameters for optimized thermoelectric Mg 2 Si, Journal of Materials Science 49 (2014) 3196–3204, https://doi.org/10.1007/s10853-014-8023-8.
[33] E.M. Godlewska, et al., Reaction and diffusion phenomena in Ag-doped Mg2Si, Journal of Alloys and Compounds 657 (2016) 755–764, https://doi.org/10.1016/j.jallcom.2015.10.174.
[34] J. de Boor, et al., Fabrication parameters for optimized thermoelectric Mg2Si, Journal of Materials Science 49 (8) (2014) 3196–3204, https://doi.org/10.1007/s10853-014-8023-8.
[35] J. de Boor, et al., Thermal Stability of Magnesium Silicide/Nickel Contacts, Journal of Electronic Materials 45 (10) (2016) 5313–5320, https://doi.org/10.1007/s11664-016-4716-x.
[36] J. de Boor, et al., Fabrication and characterization of nickel contacts for magnesium silicide based thermoelectric generators, Journal of Alloys and Compounds 632 (2015) 348–353, https://doi.org/10.1016/j.jallcom.2015.01.149.
[37] L. Cai, et al., Duration of Thermal Stability and Mechanical Properties of Mg2Si/Cu Thermoelectric Joints, Journal of Electronic Materials (2018) 47, https://doi.org/10.1007/s11664-018-6091-2.
[38] A. Ferrario, et al., Mechanical and Electrical Characterization of Low-resistivity Contact Materials for Mg2Si, Materials Today: Proceedings 2 (2) (2015) 573–582, https://doi.org/10.1016/j.matpr.2015.05.078.
[39] S. Ayachi, et al., Developing Contacting Solutions for Mg2Si1–xSnx-Based Thermoelectric Generators: Cu and Ni45Cu55 as Potential Contacting Electrodes, ACS Applied Materials & Interfaces 11 (43) (2019) 40769–40780, https://doi.org/10.1021/acsami.9b12474.
[40] J. de Boor, E. Müller, Data analysis for Seebeck coefficient measurements, Review of Scientific Instruments 84 (6) (2013) 065102, https://doi.org/10.1063/1.4807697.
[41] J. de Boor, et al., High-temperature measurement of Seebeck coefficient and electrical conductivity, Journal of Electronic Materials 42 (2013) 1711–1718, https://doi.org/10.1007/s11664-012-2404-z.
[42] K.A. Borup, et al., Measuring thermoelectric transport properties of materials, Energy & Environmental Science 8 (2) (2015) 423–435, https://doi.org/10.1039/C4EE01320D.
[43] Platzek D., et al. *Potential-Seebeck-microprobe (PSM): measuring the spatial resolution of the Seebeck coefficient and the electric potential*. in *ICT 2005. 24th International Conference on Thermoelectrics, 2005.* 2005. doi: 10.1109/ICT.2005.1519875.
[44] P. Ponnusamy, J. de Boor, E. Müller, Using the constant properties model for accurate performance estimation of thermoelectric generator elements, Applied Energy 262 (2020) 114587, https://doi.org/10.1016/j.apenergy.2020.114587.
[45] C. Goupil, Continuum theory and modeling of thermoelectric elements, John Wiley & Sons, 2015.
[46] P. Ziolkowski, P. Blaschkewitz, E. Mueller, Heat flow measurement as a key to standardization of thermoelectric generator module metrology: A comparison of reference and absolute techniques, Measurement 167 (2021) 108273, https://doi.org/10.1016/j.measurement.2020.108273.
[47] P. Ziolkowski, P. Blaschkewitz, E. Müller, Validation of commercial Bi2Te3-based thermoelectric generator modules for application as metrological reference samples, Measurement 177 (2021) 109247, https://doi.org/10.1016/j.measurement.2021.109247.
[48] P. Ziolkowski, et al., Interlaboratory Testing for High-Temperature Power Generation Characteristics of a Ni-Based Alloy Thermoelectric Module, Energy Technology 8 (11) (2020) 2000557, https://doi.org/10.1002/ente.202000557.
[49] P. Yang, et al., Analysis of peak electromagnetic torque characteristics for superconducting DC induction heaters, IEEE Access 8 (2020) 14777–14788, https://doi.org/10.1109/ACCESS.2019.2963718.

[50] J. Chen, et al., Improvement of stability in a Mg2Si-based thermoelectric single-leg device via Mg50Si15Ni50 barrier, Journal of Alloys and Compounds 926 (2022) 166888, https://doi.org/10.1016/j.jallcom.2022.166888.
[51] J. Dai, et al., Diffusion kinetics in Mg-Cu binary system, Journal of Phase Equilibria and Diffusion 36 (2015) 613–619, https://doi.org/10.1007/s11669-015-0417-z.
[52] H. Okamoto, Mg-Ni (magnesium-nickel), Journal of Phase Equilibria and Diffusion 28 (2007) 303, https://doi.org/10.1007/s11669-007-9058-1.
[53] M. Imai, Y. Isoda, H. Udono, Thermal expansion of semiconducting silicides β-FeSi2 and Mg2Si, Intermetallics 67 (2015) 75–80, https://doi.org/10.1016/j.intermet.2015.07.015.
[54] D. Kraemer, et al., High thermoelectric conversion efficiency of MgAgSb-based material with hot-pressed contacts, Energy & Environmental Science 8 (4) (2015) 1299–1308, https://doi.org/10.1039/C4EE02813A.
[55] Y. Zhu, et al., Thermodynamic criterions of the thermoelectric performance enhancement in Mg2Sn through the self-compensation vacancy, Materials Today Physics 16 (2021) 100327, https://doi.org/10.1016/j.mtphys.2020.100327.
[56] G. Skomedal, et al., High temperature oxidation of Mg2 (Si-Sn), Corrosion Science 111 (2016) 325–333, https://doi.org/10.1016/j.corsci.2016.05.016.